
Beyond Neural Activity Prediction: Probing Latent Representations in Mouse V1 Digital Twins

Adriano Lima*

Department of Psychological & Brain Sciences
University of California, Santa Barbara
Santa Barbara, CA 93117
adrianolimacotralhaa@ucsb.edu

Yuchen Hou*

Department of Computer Science
University of California, Santa Barbara
Santa Barbara, CA 93117
yuchenhou@ucsb.edu

Michael Beyeler

Department of Computer Science
Department of Psychological & Brain Sciences
University of California, Santa Barbara
Santa Barbara, CA 93117

Marius Schneider

Department of Bioengineering
University of California, Santa Barbara
Santa Barbara, CA 93117
marius_schneider@ucsb.edu

Abstract

Digital twins of sensory cortex serve as powerful response oracles for predicting neural activity to novel stimuli. Although prediction accuracy is the central metric by which these models are evaluated, it provides limited insight into the latent representations that support those predictions. This limitation becomes increasingly important as digital twins are used as *in silico* experimental systems for stimulus design and hypothesis generation: models with similar prediction accuracy may rely on different latent representations. We address this gap by systematically probing a family of convolutional-recurrent digital twins of mouse V1 trained to predict neural activity from naturalistic videos recorded in freely moving mice. The models share the same training data and neural-prediction objective, but differ in visual-encoder architecture. For each frozen model, we characterize latent representations along three levels: (i) linear decodability from controlled visual probes of orientation, contrast, and motion; (ii) latent-unit tuning to canonical visual features including orientation selectivity, contrast response, spatial-frequency tuning, and phase sensitivity; and (iii) population geometry of hidden-layer activity. Across architectures, better neural-response prediction correlates with stronger probe accuracy. Additionally, highly predictive models exhibit flatter hidden-population eigenspectra, indicating more distributed, higher-dimensional representations closer to population-geometry signatures reported in mouse V1. Although these representational properties covary with prediction accuracy across architectures, digital twins with comparable prediction scores can still differ substantially in probe performance and latent-unit tuning. These results establish multi-level representational probing as a complement to standard neural-prediction evaluation, providing a framework for understanding digital twins not only as predictors, but also as substrates for studying visual computations.

1 Introduction

Digital twins of sensory cortex are emerging as powerful response oracles. Trained on large-scale neural recordings, these models predict neural responses to novel visual stimuli and can support in

*Equal contribution.

silico stimulus design, model comparison, and hypothesis generation. In mouse primary visual cortex (V1), data-driven response models have progressed from convolutional system-identification models to larger multimodal architectures trained on natural images and naturalistic videos [Klindt et al., 2017, Lurz et al., 2021, Xu et al., 2023, Turishcheva et al., 2024b, Wang et al., 2025]. Community benchmarks such as Sensorium have accelerated this progress by comparing models primarily through held-out neural-prediction metrics, including correlations between predicted and recorded responses [Willeke et al., 2022, Turishcheva et al., 2024a, Schneider et al., 2025]. Such prediction-based evaluation is necessary: a digital twin that does not predict neural activity cannot serve as a response oracle. However, output fidelity alone does not specify what visual information the model represents, how that information is organized, or whether different high-performing models arrive at similar latent structure.

This limitation reflects a broader underdetermination problem in neural-response modeling. Multiple architectures can fit similar stimulus-response mappings while relying on different latent representations (e.g. Conwell et al. [2024]). Such differences become central when digital twins are used as in silico experimental systems to generate hypotheses about biological visual cortex or draw conclusions about sensory computation. In that setting, prediction accuracy is a necessary but incomplete evaluation criterion: we also need to know what visual computations are accessible in the model’s latent states, how individual latent units are tuned, and how population activity is organized. Importantly, while digital twins are not circuit-level mechanistic models of cortex, they are fully accessible: every hidden unit, layer, and population response can be measured under arbitrary stimuli.

A broad literature comparing networks trained on common computer vision objectives to visual cortex has shown that objective, architecture, and training data can affect how well model representations align with neural measurements [Schrimpf et al., 2018, Cadena et al., 2019, Shi et al., 2019, Nayebi et al., 2023, Conwell et al., 2024, Cadena et al., 2024]. In parallel, recent studies have begun to use data-driven neural prediction models as in silico experimental systems rather than only as response predictors. Digital twin models have been used to investigate phenomena beyond held-out neural-response prediction, including stimulus invariances, functional cell-type structure, population geometry, and hierarchical object representations [Ding et al., 2026, Burg et al., 2024, Liscai et al., 2025, Luconi et al., 2025]. Together, these studies suggest that targeted analyses of trained digital twins can reveal functional and representational structure not fully captured by prediction metrics alone.

However, there is no systematic evaluation approach to investigate what visual computations are linearly accessible, what canonical tuning properties emerge in latent units, and how hidden population activity is geometrically organized in digital twins of mouse V1. Here, we introduce a multi-level evaluation framework for probing latent representations in digital twins. We apply this framework to a family of convolutional-recurrent models trained to predict V1 activity from naturalistic video recorded in freely moving mice. The models share the same training data and neural-prediction objective but differ in their visual-encoder architecture components. This architecture sweep provides a controlled setting for systematically analyzing how visual representations are learned, testing whether improvements in neural prediction are accompanied by systematic changes in representational organization, and whether representational differences persist despite comparable output fidelity. For each frozen model, we evaluate three complementary levels: (i) linear-probe accuracy on controlled orientation, contrast, and motion-direction probes; (ii) latent-unit tuning to canonical visual dimensions (orientation selectivity, contrast response, spatial-frequency tuning, phase sensitivity); (iii) population geometry of hidden activity, summarized by the GRU eigenspectrum. These levels were chosen to connect model evaluation with interpretable descriptors from systems neuroscience and representation learning.

Across architectures, we find that neural-prediction accuracy is informative but does not fully characterize a digital twin’s internal representations. Better response predictors tend to support stronger linear readouts of orientation, contrast, and motion detection tasks, and exhibit flatter hidden-state eigenspectra closer to population-geometry signatures reported for mouse V1. Latent-unit analyses further show that response-predictive training gives rise to interpretable tuning along classical visual dimensions. Crucially, however, prediction accuracy does not uniquely determine representational organization: models with similar neural performance can differ in task accuracy, latent-unit tuning, and population geometry.

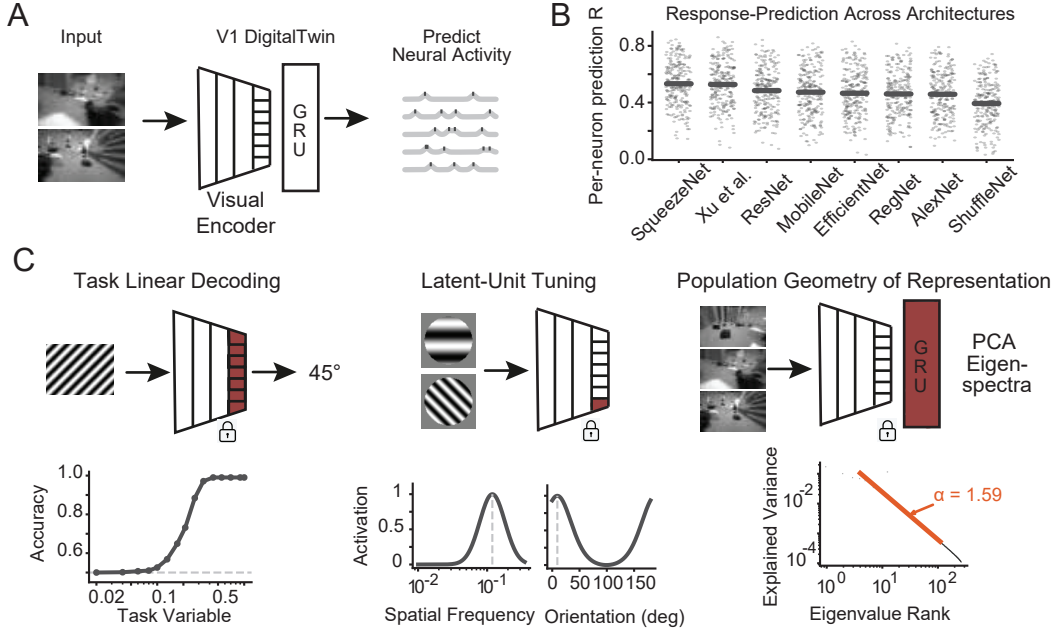


Figure 1: Multi-level probing of hidden representations in V1 digital twins. **(A)** We compare V1 digital twins trained to predict neural activity from videos recorded in freely moving mice. Models share the same neural prediction objective and differ in the visual-encoder architecture. **(B)** Held-out neural prediction performance across visual-encoder architectures. Gray points indicate per-neuron prediction correlations and horizontal bars indicate architecture means. **(C)** We characterize latent representations along three levels. Left, we measure *task decodability* by training linear readouts on controlled visual probes targeting orientation, contrast, and motion information. Middle, we estimate *latent-unit tuning* by presenting parametric stimuli and measuring responses of individual hidden units to canonical visual dimensions. Right, we quantify *population geometry* by computing the eigenspectrum of hidden-layer activity and fitting a power-law exponent α , where $\lambda_k \propto k^{-\alpha}$.

Our contributions are: First, we systematically probe the latent representations of convolutional–recurrent digital twins of mouse V1 along three levels: linear-probe task readouts, latent-unit tuning, and population geometry, using twins trained for neural prediction. Second, we show that several representational properties (linear decodability of low-level visual information, classical tuning structure, and population-geometry signatures of mouse V1) emerge with the prediction objective and covary with prediction quality across architectures. Third, we establish multi-level representational probing as a complement to neural prediction metrics, providing an evaluation strategy for comparing digital twins not only by how accurately they predict neural responses, but also by what their latent representations make available for in silico analysis.

2 Methods

We evaluated whether neural-prediction models of mouse primary visual cortex learn representations that support mouse-relevant visual computations. The analysis pipeline contained five substantive components, with frozen feature extraction serving as the bridge from trained neural-prediction models to downstream probes. First, we trained a family of multi-mouse V1 neural-prediction models based on the freely moving digital-twin architecture of Xu et al. [2023]. The recurrent component was held fixed while the visual encoder was varied (§2.1). Second, we froze each trained model and extracted fixed representations for downstream analysis (§2.1). Third, we trained linear probes on synthetic visual tasks designed to measure task-relevant information in the learned representation (§2.2). Fourth, we characterized emergent feature tuning using parametric gratings and quantified hidden representation geometry using PCA eigenspectra (§2.3). Finally, we related neural-prediction performance, behavioral readout performance, population geometry, and tuning summaries across

models using cross-model scatter and regression analyses (Appendix A.5). Detailed architecture, training, task, feature-extraction, tuning, and statistical-analysis settings are provided in Appendix A.

2.1 Neural-prediction training and frozen feature extraction

Model family and encoder architectures. We trained a family of convolutional-recurrent neural-prediction models on mouse V1 activity. Each model mapped grayscale movie frames through a visual encoder, integrated the resulting feature sequence with a single-layer GRU, and predicted neural activity with mouse-specific readout heads. The visual encoder and GRU were shared across mice, whereas the final readout heads were mouse-specific. The primary model variation was the visual encoder family, while recurrent integration, mouse-specific readout structure, and the training objective were held fixed to systematically analyze how visual representations learned under neural-prediction training. The encoder family comprised CNN, ResNet-18, EfficientNet-B0, MobileNet-V2, AlexNet, SqueezeNet-1.1, ShuffleNet-V2, and RegNet-Y-400MF; detailed architecture settings are provided in Appendix A.2.

Neural data, training, and frozen features. Models were trained jointly on publicly available neural-response recordings from three mice freely running in an arena (see Parker et al. [2022]). Each session was represented as temporally ordered movie frames paired with simultaneous V1 single-neuron activity. Training examples were five-frame grayscale clips with a 48 ms sampling rate, and each target was the neural response at the next time bin. Each encoder architecture was trained across three run seeds, and for each architecture-seed pair we retained the checkpoint with the best validation objective.

A task-specific linear probe was trained on frozen model latent features for downstream representational analyses. Feature extraction was matched to the temporal structure of each task. Static orientation discrimination task used 108-dimensional visual-encoder outputs from single-frame stimuli. Dynamic Contrast and Motion RDK tasks used 512-dimensional GRU hidden-state features after recurrent temporal integration. Linear probes were trained on these frozen features using matched synthetic stimulus draws across architectures within each run seed.

2.2 Behavioral readout tasks

The behavioral readout suite probed three synthetic visual computations not used in neural-prediction training: static grating orientation, flashed-target contrast detection, and coherent-motion direction discrimination. See A.3 for details.

Orientation task was an eight-way static grating classification task. Each trial was a single full-field sinusoidal grating with orientation sampled from one of eight bins spanning $[0^\circ, 180^\circ)$. Performance was classification accuracy over a training-size sweep, with accuracy at the largest training-set size used as the scalar endpoint.

Dynamic Contrast task was a binary target-detection task using five-frame clips. On positive trials, a Gabor target was flashed in a fixed visual-field patch; on negative trials, the clip contained only noisy background. Probes were evaluated across target contrasts from blank or near-blank stimuli through high contrast. Performance at each contrast was summarized by balanced accuracy, and the primary endpoint was the area under the balanced-accuracy curve.

Motion RDK task was a two-alternative direction-discrimination task using 80-frame random-dot kinematogram clips. Probes were trained on high-coherence conditions and evaluated on a coherence grid from chance-level motion through high-coherence stimuli. Clips were processed in five-frame chunks, and the final chunk’s GRU hidden state was used as the clip-level feature. The primary endpoint was the area under the accuracy-versus-coherence curve.

2.3 Emergent tuning and representation geometry

We measured latent tuning at the final visual-encoder output by presenting static full-field sinusoidal gratings to each frozen encoder. Treating each output dimension as a latent feature unit, we summarized orientation selectivity, phase modulation, spatial-frequency preference, and signed contrast-response tuning for cross-model analyses. In addition, we quantified latent representation geometry using the eigenspectrum of GRU hidden activity. For each trained model, we extracted final

GRU hidden states from 5,000 clips of a fixed reference mouse session, computed PCA eigenspectra, and fit a power-law exponent over ranks 20-200. The resulting GRU eigenspectrum exponent was used as the representation-geometry summary in the cross-model analyses.

3 Results

3.1 A multi-level framework for probing V1 digital-twin representations

Digital twins are typically optimized and evaluated as neural response predictors. This output-level evaluation does not specify what information is represented in the model’s latent states. To characterize these learned representations directly, we evaluated digital twins along multiple levels alongside the neural prediction accuracy.

We trained eight convolutional-recurrent models to predict V1 activity from naturalistic videos recorded in freely moving mice (Fig. 1A). Across architectures, the models achieved comparable held-out prediction performance, establishing that each model could serve as a response oracle while also exhibiting measurable differences in output fidelity (Fig. 1B).

We then probed the latent representation of the tested visual encoders along three levels (Fig. 1C). First, we measured *linear functional access*: whether information about controlled visual variables could be recovered from frozen latent features using simple linear readouts. We used three probes targeting orientation, contrast, and motion information to provide controlled assays of visual computations that are classically relevant for mouse V1 and can be compared across digital twins.

Second, we quantified *latent-unit tuning*. Using parametric stimuli, we measured responses of individual latent units to orientation selectivity, contrast response, spatial frequency tuning, and phase sensitivity. This analysis investigates whether the models’ individual units develop interpretable selectivity along visual dimensions commonly used to characterize V1 responses.

Third, we measured *population-level geometry* of hidden-layer activity. For each model, we computed the eigenspectrum of population responses to naturalistic stimuli and fit a power-law exponent α to summarize how variance is distributed across population dimensions. This provides a global descriptor of representational organization that complements the unit-level tuning analysis. These three levels allow us to separate output fidelity from representational properties, which will be analyzed in detail in the following sections.

3.2 Controlled visual probes reveal linear functional access in V1 digital twins

Linear readouts recover task-relevant information across architectures. To assess what visual information is linearly decodable from the latent representations of V1 digital twins, we froze each model’s latent features and trained simple linear readouts on three controlled visual probes targeting orientation, dynamic contrast, and motion information (Fig. 2A, S. Table 2).

All architectures supported non-trivial linear readout performance on two of the three probes, but the level of accessible information differed substantially across models (Fig. 2B, top). For the orientation probe, readout accuracy was considerably above chance even at very small training sample sizes, indicating that frozen latent representations contain recoverable information about orientation. However, the performance of this readout varied across architectures, with some models reaching substantially higher accuracy than others (e.g., 0.411 ± 0.052 in ShuffleNet vs. 0.776 ± 0.022 in Xu et al. [2023]). For the dynamic contrast probe, all models exhibited psychometric-like performance curves, with balanced accuracy increasing as contrast increased, but again with clear differences in slope and saturation across architectures. For the motion-direction probe based on random-dot kinematograms (RDKs), performance remained closer to chance overall, indicating that motion information was less accessible than orientation or contrast in these frozen representations. Nonetheless, a subset of models (e.g., 0.562 ± 0.022 in SqueezeNet and 0.545 ± 0.009 in AlexNet) showed clearly elevated, coherence-dependent readout while most remained close to chance, indicating that direction-discrimination accessibility is not uniform across the model family.

Task performance covaries with neural prediction across architectures. To summarize these differences, we computed a scalar performance metric for each probe and related it to held-out neural prediction accuracy across architectures (Fig. 2B, bottom). For orientation, we used out-of-distribution

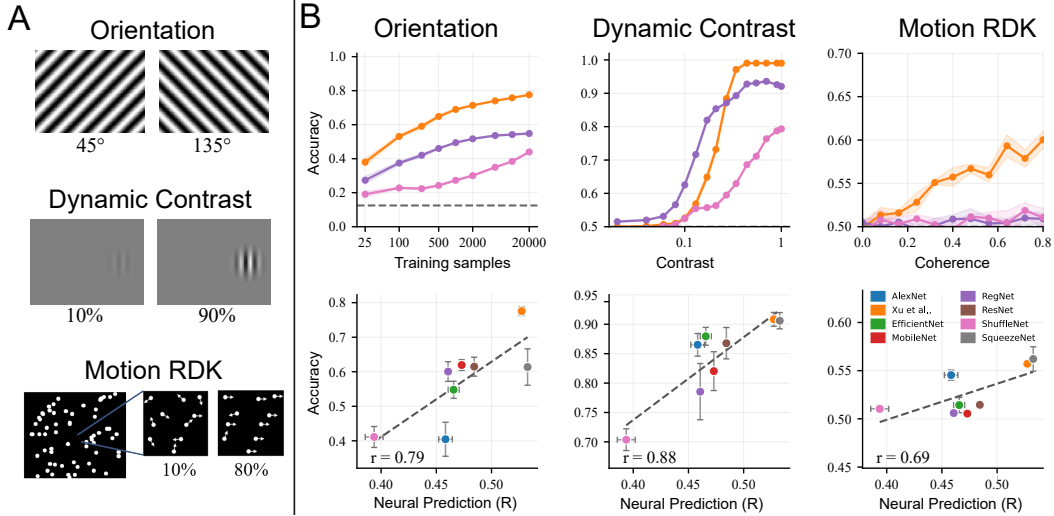


Figure 2: **Controlled visual probes reveal functional access in V1 digital twins.** (A) Example stimuli for the three controlled visual probes: orientation discrimination, dynamic contrast detection, and RDK motion-direction discrimination. (B) Linear readout performance across visual-encoder architectures. Top: representative task-performance curves for each probe. Bottom: architecture-level relationships between probe performance and held-out neural prediction accuracy. Points indicate architecture means with seed variability; correlations are computed across architecture means.

accuracy at the largest training-set size; for dynamic contrast, balanced-accuracy AUC across contrast levels; and for RDKs, accuracy AUC across motion coherence. Across architecture means ($n = 8$), models with better neural prediction tended to also support stronger linear readouts on all three probes. This relationship was strongest for dynamic contrast detection ($r = 0.88$, $p = 0.0037$) and orientation discrimination ($r = 0.79$, $p = 0.0209$), and weaker for motion-direction discrimination ($r = 0.69$, $p = 0.0606$), where the trend was preserved but marginally below significance.

However, architectures with comparable neural-prediction performance can occupy different positions on each task readout. For example, both Xu et al. [2023] and SqueezeNet have similar neural prediction scores (0.527 ± 0.154 and 0.533 ± 0.157), and perform similarly in dynamic contrast (0.908 ± 0.020 and 0.906 ± 0.024), but have substantially different orientation-probe accuracy (0.776 ± 0.022 and 0.614 ± 0.091). This discrepancy suggests that prediction accuracy reflects, but does not fully determine, the functional structure of twin representations.

3.3 Latent-unit tuning provides interpretable but partial axes of functional access

The controlled probes in Fig. 2 show that the visual information accessible from frozen digital-twin representations varies across architectures. We then tested whether these differences are reflected in the tuning properties of individual latent units. Using parametric visual stimuli, we measured tuning to canonical visual dimensions commonly used to characterize V1 responses [Niell and Stryker, 2008]. More specifically, for each architecture, we summarized latent-unit responses using global orientation selectivity (gOSI), contrast-response parameters (C_{50}), preferred spatial frequency, and phase sensitivity (F1/F0). C_{50} denotes the contrast at which the fitted response reaches half its saturating amplitude, and F1/F0 quantifies phase sensitivity, with larger values indicating stronger phase modulation and smaller values indicating more phase-invariant responses.

Latent units exhibited structured tuning along all measured visual dimensions (Fig. 3A, B). Individual units showed orientation-selective responses, contrast-dependent response profiles, spatial-frequency preferences, and phase-dependent modulation. Across architectures, the distributions of these descriptors differed, indicating that models trained with the same neural-prediction objective can nevertheless develop distinct unit-level response profiles. However, most models shared moderate orientation selectivity (0.297 ± 0.085) and low spatial-frequency preferences (0.126 ± 0.050 cycle-per-pixel, equivalent to 0.084 ± 0.033 cycle-per-degree), which were broadly compatible with values reported for mouse V1 under grating stimulation [Niell and Stryker, 2008]. Note that we use these

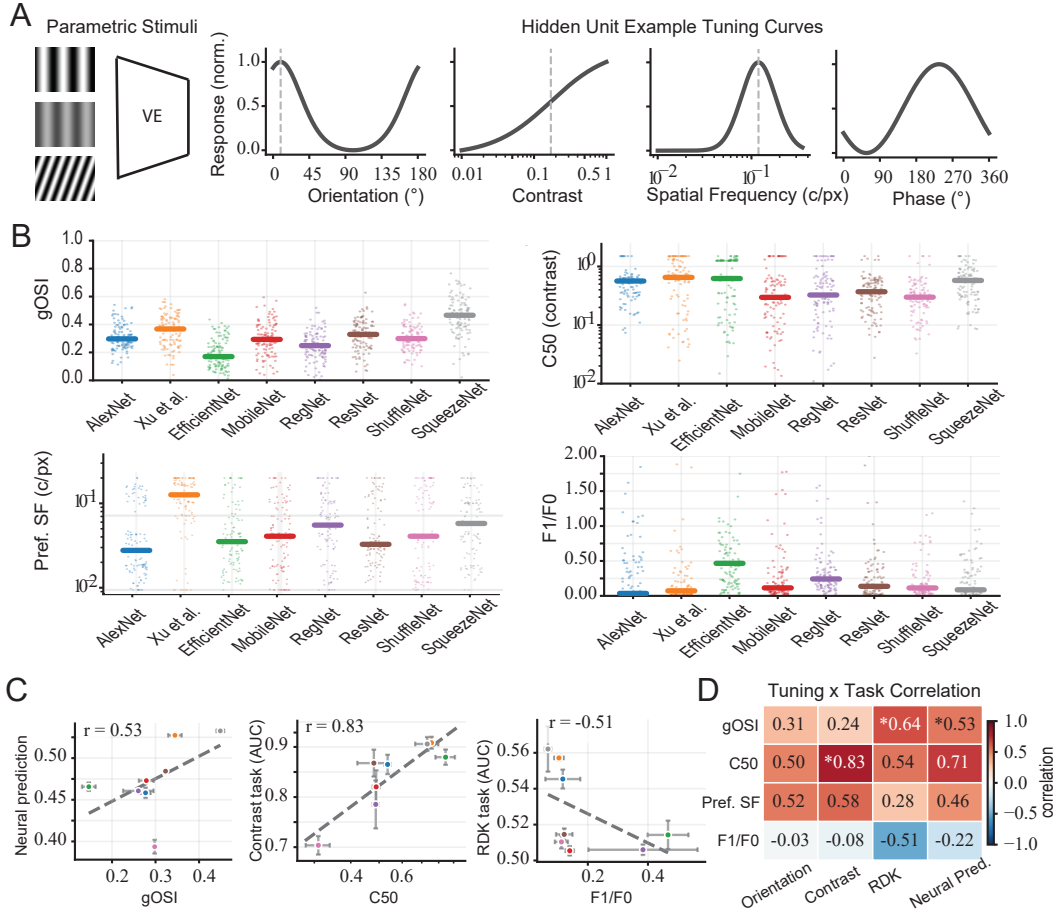


Figure 3: Latent-unit tuning provides interpretable axes for comparing V1 digital twins. (A) We probed latent units with parametric visual stimuli varying canonical stimulus dimensions, including orientation, contrast, spatial frequency, and phase. Example latent units show structured responses to orientation, contrast, and spatial frequency, from which we derived tuning metrics such as global orientation selectivity (gOSI), contrast semisaturation (C_{50}), preferred spatial frequency, and phase modulation (F1/F0). (B) Distributions of latent-unit tuning metrics across visual-encoder architectures. Points indicate individual hidden units and horizontal bars indicate architecture-level medians. (C) Selected architecture-level relationships between tuning metrics and neural prediction or functional readout performance. Points indicate architecture means with seed variability shown where available; correlations are computed across architecture means. (D) Architecture-level correlations between tuning metrics and controlled visual probes or neural prediction performance. * $p < 0.05$. Cluster Robust OLS on seed-level data, clustering by architecture ($n = 8$ architectures, 3 random seeds each).

comparisons as biological reference ranges, not as evidence of one-to-one equivalence between hidden units and cortical neurons.

We then explored whether these tuning properties relate to task performance (Fig. 3C, D). Orientation-probe performance marginally correlated with global orientation selectivity gOSI ($r = 0.31, p = 0.053$). Contrast-probe performance was most strongly associated with the contrast-response midpoint C_{50} ($r = 0.83, p = 0.002$), indicating that C_{50} was the tuning property most directly relevant to contrast sensitivity. Motion-direction performance in the RDK probe was associated with gOSI ($r = 0.64, p = 0.006$) and showed a marginal negative correlation with the phase sensitivity index F1/F0 ($r = -0.51, p = 0.056$). These relationships suggest that latent-unit tuning provides interpretable information for understanding downstream visual tasks, and that no individual tuning statistic fully determines all task performance.

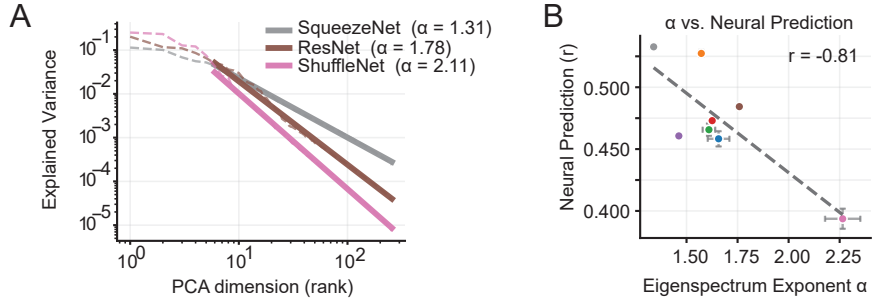


Figure 4: **Population geometry of hidden representations covaries with neural prediction performance.** (A) Example eigenspectra of latent-layer activity for three visual-encoder architectures. For each model, hidden activations were collected across naturalistic video stimuli, decomposed with PCA, and summarized by the eigenspectrum of explained variance. Solid lines show power-law fits, $\lambda_k \propto k^{-\alpha}$, over the fitted rank range; lower α corresponds to a flatter spectrum with variance distributed across more population dimensions. (B) Eigenspectrum exponent α is negatively associated with held-out neural prediction performance across architectures. Points show architecture means and error bars indicate variability across seeds; the correlation is computed across architecture means.

3.4 Population geometry of hidden activity covaries with neural prediction accuracy

To characterize organization beyond individual hidden units, we used the eigenspectrum of hidden-layer activity to quantify population geometry. For each architecture, we collected hidden states in response to naturalistic video inputs, computed the covariance matrix of the resulting population activity, and fit a power law, $\lambda_k \propto k^{-\alpha}$, over a fixed range of principal-component ranks. The exponent α summarizes how variance decays across dimensions: larger α indicates activity dominated by a few dimensions, smaller α means a flatter, higher-dimensional representation. Stringer et al. [2019] showed that mouse V1 responses to high-dimensional natural images exhibit approximately power-law eigenspectra with exponents close to 1: high-dimensional enough to be expressive, yet structured enough to support smooth stimulus representations.

Recent work has applied this descriptor to digital twins at the level of predicted neural responses, revealing that twins can achieve high single-neuron prediction while failing to reproduce biological population geometry [Liscai et al., 2025]. We instead apply the descriptor to the hidden representations that produce these predictions, to explore whether the latent population geometry varies systematically with prediction quality across architectures.

Overall, the fitted exponents were steeper than the values reported for mouse V1 (Fig.4A), indicating that hidden activity remained more concentrated in leading dimensions than biological V1 population responses. However, architectures with better neural prediction accuracy tended to have lower α , corresponding to flatter and more distributed hidden population activity closer to population-geometry signatures reported for mouse V1 ($r = -0.81, p < 0.001$, Fig.4B). Among the representational descriptors we measured, α showed one of the strongest associations with neural prediction performance. Together, these results show that eigenspectrum analysis provides a population-level descriptor of hidden representations that complements both neural prediction accuracy and hidden-unit tuning.

4 Discussion and Limitations

Digital twins of sensory cortex are built to predict neural responses, and prediction accuracy is therefore the central metric for evaluating their success as response oracles. Here, we ask a complementary question: what hidden representations do these response oracles develop? We characterized latent representations in a family of V1 digital twins trained with the same neural-prediction objective but different visual-encoder architectures. We evaluated their latent representations using three complementary probes: linear readouts measured which low-level visual variables were linearly accessible from frozen latent states, tuning analyses described how individual latent units responded to canonical stimulus dimensions, and eigenspectra summarized the population-level organization

of hidden activity. Because no task- or tuning-related objective was used during training, these analyses could reveal what representational structure emerges from neural-response prediction alone. Across the architectures tested, stronger neural prediction was associated with stronger readouts in orientation, contrast, and motion information, as well as flatter, more distributed population eigen-spectra. Latent-unit tuning provided interpretable descriptors along classical visual dimensions and revealed architecture-dependent differences in unit-level response properties. Together, these results establish representational characterization as a complementary way to compare V1 digital twins beyond prediction accuracy alone.

Prediction accuracy underdetermines representation. The flexibility that makes modern digital twins effective response predictors also makes their internal organization underdetermined: high-capacity architectures can fit similar stimulus-response mappings while converging to different latent representations. This matters when digital twins are used as scientific instruments rather than only as response oracles, because two models with comparable prediction accuracy can fail on different stimulus regimes, support different downstream computations, or learn distinct intermediate representations of the same input. Unlike the biological circuits whose stimulus-response mapping they approximate, digital twins provide direct access to their internal states; every latent feature can be measured and perturbed under controlled stimulus conditions. Representational probing therefore turns underdetermination from a limitation into a question that can be answered empirically: which representational differences persist among well-predicting twins, and which level do those differences covary along? Our results suggest that better prediction is accompanied by stronger functional readouts and more V1-like population geometry, while meaningful representational differences remain among models with similar prediction scores.

Population geometry in hidden representations. Among the three representational levels, population geometry showed the strongest association with prediction accuracy, with better predictors exhibiting lower α and more distributed hidden activity. This complements work on population geometry at the level of predicted neural responses: Liscai et al. [2025] found that output-stage geometry can diverge from biological V1 even when single-neuron prediction is strong, and that shifting output geometry toward biological V1 requires additional regularization and decreases prediction accuracy. At the level of hidden states, we observe that higher prediction accuracy was associated with hidden-population geometry shifted toward (though not reaching) the V1 regime, despite no explicit population-geometry objective.

Limitations. Our analysis covers eight visual-encoder architectures trained within the same convolutional-recurrent digital-twin framework, on the same freely moving mouse V1 dataset, and with the same neural-prediction objective. This design isolates architectural variation within one model family, but it does not cover the full design space of digital twins, including transformer-based or otherwise substantially different architectures. The cross-architecture relationships should therefore be interpreted as descriptive trends within the tested model family. A larger architectural sweep will be needed to determine whether the relationships between prediction accuracy, functional access, tuning, and population geometry generalize across broader classes of neural-response models.

Future directions. Our evaluation method can be used to address questions that are not captured by aggregate prediction scores. First, applying the probes across layers would reveal how visual information, tuning, and population geometry are built across the hierarchy of a digital twin. Second, applying the framework across model families, datasets, and training objectives would test whether different digital twins converge to distinct representations with similar output performance. Third, two twins with similar averaged scores may fail on different stimulus regimes or predict different subsets of neurons well. Testing whether the error profiles can be predicted from a model’s representations would make hidden-state analysis directly useful for digital twin selection.

Conclusion. Digital twins are built to predict neural responses, and prediction accuracy remains the central measure of their value as response oracles. Our results show that models with the same neural-prediction objective can differ in controlled-probe performance, latent-unit tuning, and population geometry. These differences are related to prediction quality, but they are not summarized by a single prediction correlation score. The latent representations of digital twins therefore deserve direct evaluation: they reveal what visual structure emerges from neural-response prediction, and provide a basis for comparing digital twins beyond accuracy.

Data and Code Availability. The neural recording data used to train and evaluate the digital twins is publicly available through osf.io. All code, including model training, analyses, and evaluation pipeline, will be publicly available upon publication.

References

- Max F. Burg, Thomas Zenkel, Michaela Vystrcilova, Jonathan Oesterle, Larissa Hoffling, Konstantin F. Willeke, Jan Lause, Sarah Mueller, Paul G. Fahey, Zhiwei Ding, Kelli Restivo, Shashwat Sridhar, Tim Gollisch, Philipp Berens, Andreas S. Tolias, Thomas Euler, Matthias Bethge, and Alexander S. Ecker. Most discriminative stimuli for functional cell type clustering. In *International Conference on Learning Representations*, 2024. URL <https://openreview.net/forum?id=9W6KaAcYlr>.
- Santiago A. Cadena, Fabian H. Sinz, Taliah Muhammad, Emmanouil Froudarakis, Erick Cobos, Edgar Y. Walker, Jacob Reimer, Matthias Bethge, Andreas S. Tolias, and Alexander S. Ecker. How well do deep neural networks trained on object recognition characterize the mouse visual system? In *Real Neurons & Hidden Units Workshop at NeurIPS*, 2019. URL <https://openreview.net/forum?id=rkxcXmtUUS>.
- Santiago A. Cadena, Konstantin F. Willeke, Kelli Restivo, George Denfield, Fabian H. Sinz, Matthias Bethge, Andreas S. Tolias, and Alexander S. Ecker. Diverse task-driven modeling of macaque V4 reveals functional specialization towards semantic tasks. *PLOS Computational Biology*, 20(5):e1012056, 2024. doi: 10.1371/journal.pcbi.1012056. URL <https://journals.plos.org/ploscompbiol/article?id=10.1371/journal.pcbi.1012056>.
- Colin Conwell, Jacob S. Prince, Kendrick N. Kay, George A. Alvarez, and Talia Konkle. A large-scale examination of inductive biases shaping high-level visual representation in brains and machines. *Nature Communications*, 15:9383, 2024. doi: 10.1038/s41467-024-53147-y. URL <https://www.nature.com/articles/s41467-024-53147-y>.
- Zhiwei Ding, Dat Tran, Kayla Ponder, et al. Functional bipartite invariance in mouse primary visual cortex receptive fields. *Nature Neuroscience*, 2026. doi: 10.1038/s41593-026-02213-3. URL <https://www.nature.com/articles/s41593-026-02213-3>.
- Lindsey L. Glickfeld, Mark H. Histed, and John H. R. Maunsell. Mouse primary visual cortex is used to detect both orientation and contrast changes. *Journal of Neuroscience*, 33(50):19416–19422, 2013. doi: 10.1523/JNEUROSCI.3560-13.2013. URL <https://www.jneurosci.org/content/33/50/19416>.
- Hojin Jang and Frank Tong. Improved modeling of human vision by incorporating robustness to blur in convolutional neural networks. *Nature Communications*, 15:1989, 2024. doi: 10.1038/s41467-024-45679-0. URL <https://www.nature.com/articles/s41467-024-45679-0>.
- David A. Klindt, Alexander S. Ecker, Thomas Euler, and Matthias Bethge. Neural system identification for large populations separating “what” and “where”. In *Advances in Neural Information Processing Systems 30*, pages 3507–3517, 2017. URL https://proceedings.neurips.cc/paper_files/paper/2017/file/8c249675aea6c3cbd91661bbae767ff1-Paper.pdf.
- Dario Liscai, Emanuele Luconi, Alessandro Marin Vargas, and Alessandro Sanzeni. Beyond single neurons: population response geometry in digital twins of mouse visual cortex. In *International Conference on Learning Representations*, 2025. URL <https://openreview.net/forum?id=kSISSDUYFh>.
- Emanuele Luconi, Dario Liscai, Carlo Baldassi, Alessandro Marin Vargas, and Alessandro Sanzeni. Anatomically inspired digital twins capture hierarchical object representations in visual cortex. In *Advances in Neural Information Processing Systems*, 2025. URL <https://openreview.net/forum?id=9DbkBqvCI>.
- Konstantin-Klemens Lurz, Mohammad Bashiri, Konstantin Willeke, Akshay Jagadish, Eric Wang, Edgar Y. Walker, Santiago A. Cadena, Taliah Muhammad, Erick Cobos, Andreas S. Tolias, Alexander S. Ecker, and Fabian H. Sinz. Generalization in data-driven models of primary visual cortex. In *International Conference on Learning Representations*, 2021. URL <https://openreview.net/forum?id=Tp7kI90Htd>.
- Aran Nayebi, Nathan C. L. Kong, Chengxu Zhuang, Justin L. Gardner, Anthony M. Norcia, and Daniel L. K. Yamins. Mouse visual cortex as a limited resource system that self-learns an ecologically-general representation. *PLOS Computational Biology*, 19(10):e1011506, 2023. doi: 10.1371/journal.pcbi.1011506. URL <https://journals.plos.org/ploscompbiol/article?id=10.1371/journal.pcbi.1011506>.

- Cristopher M. Niell and Michael P. Stryker. Highly Selective Receptive Fields in Mouse Visual Cortex. *The Journal of Neuroscience*, 28(30):7520–7536, July 2008. ISSN 0270-6474, 1529-2401. doi: 10.1523/JNEUROSCI.0623-08.2008. URL <https://www.jneurosci.org/lookup/doi/10.1523/JNEUROSCI.0623-08.2008>.
- Philip R. L. Parker, Elliott T. T. Abe, Emmalyn S. P. Leonard, Dylan M. Martins, and Cristopher M. Niell. Joint coding of visual input and eye/head position in V1 of freely moving mice. *Neuron*, 110(23):3897–3906.e5, December 2022. ISSN 0896-6273. doi: 10.1016/j.neuron.2022.08.029. URL <https://www.sciencedirect.com/science/article/pii/S0896627322008042>.
- Dario L. Ringach, Patrick J. Mineault, Elaine Tring, Nicholas D. Olivas, Pablo Garcia-Junco-Clemente, and Joshua T. Trachtenberg. Spatial clustering of tuning in mouse primary visual cortex. *Nature Communications*, 7:12270, 2016. doi: 10.1038/ncomms12270. URL <https://www.nature.com/articles/ncomms12270>.
- Marius Schneider, Joe Canzano, Jing Peng, Yuchen Hou, Spencer LaVere Smith, and Michael Beyeler. Mouse vs. AI: A Neuroethological Benchmark for Visual Robustness and Neural Alignment, September 2025. URL <http://arxiv.org/abs/2509.14446>. arXiv:2509.14446 [q-bio].
- Martin Schrimpf, Jonas Kubilius, Ha Hong, Najib J. Majaj, Rishi Rajalingham, Elias B. Issa, Kohitij Kar, Pouya Bashivan, Jonathan Prescott-Roy, Kailyn Schmidt, Daniel L. K. Yamins, and James J. DiCarlo. Brain-score: Which artificial neural network for object recognition is most brain-like? *bioRxiv*, 2018. doi: 10.1101/407007. URL <https://www.biorxiv.org/content/10.1101/407007v1>.
- Jianghong Shi, Eric Shea-Brown, and Michael A. Buice. Comparison against task-driven artificial neural networks reveals functional organization of mouse visual cortex. In *Advances in Neural Information Processing Systems*, 2019. doi: 10.48550/arXiv.1911.07986. URL <https://arxiv.org/abs/1911.07986>.
- Jeffrey N. Stirman, Leah B. Townsend, and Spencer L. Smith. A touchscreen based global motion perception task for mice. *Vision Research*, 127:74–83, 2016. doi: 10.1016/j.visres.2016.07.006. URL <https://pubmed.ncbi.nlm.nih.gov/27497283/>.
- Carsen Stringer, Marius Pachitariu, Nicholas Steinmetz, Matteo Carandini, and Kenneth D Harris. High-dimensional geometry of population responses in visual cortex. *Nature*, 571(7765):361–365, 2019.
- Polina Turishcheva, Max F. Burg, Fabian H. Sinz, and Alexander S. Ecker. Reproducibility of predictive networks for mouse visual cortex. In *Advances in Neural Information Processing Systems 37*, 2024a. URL <https://arxiv.org/abs/2406.12625>.
- Polina Turishcheva, Paul G. Fahey, Laura Hansel, Rachel Froebe, Kayla Ponder, Michaela Vystreilova, Konstantin F. Willeke, Mohammad Bashiri, Eric Wang, Zhiwei Ding, Andreas S. Tolias, Fabian H. Sinz, and Alexander S. Ecker. The dynamic sensorium competition for predicting large-scale mouse visual cortex activity from videos, 2024b. URL <https://arxiv.org/abs/2305.19654>. arXiv:2305.19654.
- Eric Y. Wang, Paul G. Fahey, Zhuokun Ding, Stelios Papadopoulos, Kayla Ponder, Marissa A. Weis, Andersen Chang, Taliah Muhammad, Saumil Patel, Zhiwei Ding, Dat Tran, Jiakun Fu, Casey M. Schneider-Mizell, MICrONS Consortium, et al. Foundation model of neural activity predicts response to new stimulus types. *Nature*, 640(8058):470–477, 2025. doi: 10.1038/s41586-025-08829-y. URL <https://www.nature.com/articles/s41586-025-08829-y>.
- Konstantin F. Willeke, Paul G. Fahey, Mohammad Bashiri, Laura Pede, Max F. Burg, Christoph Blessing, Santiago A. Cadena, Zhiwei Ding, Konstantin-Klemens Lurz, Kayla Ponder, Taliah Muhammad, Saumil S. Patel, Alexander S. Ecker, Andreas S. Tolias, and Fabian H. Sinz. The Sensorium competition on predicting large-scale mouse primary visual cortex activity, 2022. URL <https://arxiv.org/abs/2206.08666>.
- Aiwen Xu, Yuchen Hou, Cris M. Niell, and Michael Beyeler. Multimodal deep learning model unveils behavioral dynamics of V1 activity in freely moving mice. In *Advances in Neural Information Processing Systems 36*, pages 15341–15357, 2023. URL <https://openreview.net/forum?id=qv5UZJTnda>.

A Detailed Methods

A.1 Neural-prediction training details

Mouse sessions. We used publicly available freely moving neural recordings from Parker et al. [2022], which are accessible through osf.io/msp3a/overview. The neural-prediction models were trained jointly on three mouse V1 sessions: 070921_J553RT, 110421_J569LT, and 101521_J559NC. Following Xu et al. [2023], for each session, data were organized into ten temporal segments. Training used the session-specific training split from each segment, with the first 80% of each segment used for optimization and the remaining 20% used for validation. Test-split segments were held out for downstream neural-prediction evaluation. In the current multi-mouse training pipeline, all recorded units are retained for each mouse-specific readout.

Dataset construction. For a mouse m , each training example consisted of a movie snippet $\mathbf{x}_{t:t+4}^{(m)} \in \mathbb{R}^{5 \times 1 \times 60 \times 80}$ and a neural-response target $\mathbf{y}_{t+5}^{(m)} \in \mathbb{R}^{N_m}$, where N_m is the number of recorded units for mouse m . Movie arrays were converted to single-channel tensors and normalized to $[0, 1]$ by subtracting the movie minimum and dividing by the movie maximum when positive. The training dataloaders cycled through the three mice and updated the shared visual encoder and GRU together with the active mouse’s readout head.

Architecture. Each frame was processed independently by the shared visual encoder f_θ , producing a sequence of feature vectors

$$\mathbf{z}_{t+i} = f_\theta(\mathbf{x}_{t+i}) \in \mathbb{R}^{108}, \quad i = 0, \dots, 4.$$

The sequence $(\mathbf{z}_t, \dots, \mathbf{z}_{t+4})$ was then passed to a single-layer GRU with hidden size 512. The final hidden state $\mathbf{h}_{t+4} \in \mathbb{R}^{512}$ was mapped to neural responses by a mouse-specific linear readout $W_m \mathbf{h}_{t+4} + \mathbf{b}_m$ followed by a softplus nonlinearity:

$$\hat{\mathbf{y}}_{t+5}^{(m)} = \text{softplus}(W_m \mathbf{h}_{t+4} + \mathbf{b}_m).$$

The visual encoder and GRU parameters were shared across all mice, whereas the readout matrices W_m and biases \mathbf{b}_m were separate for each mouse.

Loss. For each minibatch from mouse m , the primary loss was Poisson negative log-likelihood with non-log predictions,

$$\mathcal{L}_{\text{Poisson}} = \frac{1}{BN_m} \sum_{b=1}^B \sum_{j=1}^{N_m} \left(\hat{y}_{bj}^{(m)} - y_{bj}^{(m)} \log \hat{y}_{bj}^{(m)} \right),$$

with the constant term omitted. We added an L1 penalty on the active mouse’s readout weights,

$$\mathcal{L} = \mathcal{L}_{\text{Poisson}} + \lambda_{\text{L1}} \frac{\|W_m\|_1}{|W_m|},$$

where $\lambda_{\text{L1}} = 1.0$ and $|W_m|$ denotes the number of elements in that readout matrix.

Optimization. Training used AdamW with minibatches of 256 sequences and at most 100 epochs. The visual encoder, GRU, and readout heads used separate optimizer parameter groups: visual encoder learning rate 2×10^{-4} and weight decay 10^{-5} ; GRU learning rate 10^{-4} and weight decay 10^{-6} ; readout-head learning rate 10^{-3} and no weight decay. Gradients were clipped to a maximum norm of 1.0. A ReduceLROnPlateau scheduler monitored the validation objective, using reduction factor 0.5, patience 2, and minimum learning rate 10^{-6} . Training stopped early after five epochs without validation improvement. Each encoder architecture was trained across three run seeds, and the best-validation checkpoint was saved separately for each encoder architecture and run seed.

Neural-prediction evaluation. After training, each model was evaluated separately on each mouse’s held-out test segments. Neural-prediction performance was summarized by Pearson correlation between predicted and recorded responses, computed both as per-neuron correlations and as an overall correlation across all predicted and observed response entries. For the per-neuron metric, correlations were first computed within non-overlapping 100-sample chunks for each neuron, averaged across chunks within each neuron, and then averaged across neurons. These neural-prediction metrics were used as one axis of the cross-model analyses.

A.2 Visual encoder architectures

Model label	Visual encoder	Modification
CNN [Xu et al., 2023]	Original three-block convolutional encoder with channel widths $1 \rightarrow 128 \rightarrow 64 \rightarrow 32$, kernel size 7, stride 2, batch normalization, ReLU nonlinearities, dropout, flattening, and a final linear projection.	Trained within the neural-prediction pipeline; architecture matches the original Xu et al. encoder except for the shared 108-dimensional output.
ResNet	ResNet-18.	First convolution replaced by a one-channel grayscale stem; final fully connected layer replaced by a 108-output linear layer.
EfficientNet	EfficientNet-B0.	Convolutional stem replaced for one-channel grayscale input; classifier replaced by a 108-output linear layer.
MobileNet	MobileNet-V2.	First convolution replaced for one-channel grayscale input; classifier output replaced by a 108-output linear layer.
AlexNet	AlexNet.	First convolution replaced for one-channel grayscale input; classifier modified to map the resulting feature map to 108 outputs. Final max-pooling operation removed to accommodate the smaller input resolution.
SqueezeNet	SqueezeNet-1.1.	First convolution replaced for one-channel grayscale input; final classifier convolution replaced to output 108 channels before global pooling.
ShuffleNet	ShuffleNet-V2 1.0x.	Initial convolution replaced for one-channel grayscale input; final fully connected layer replaced by a 108-output linear layer.
RegNet	RegNet-Y-400MF.	Stem convolution replaced for one-channel grayscale input; final fully connected layer replaced by a 108-output linear layer.

Table 1: Visual encoder architectures used in neural-prediction. All encoders output a 108-dimensional vector per frame, which is then passed to the same single-layer GRU with hidden size 512 and mouse-specific neural readouts. Standard image-model backbones were modified to accept one-channel grayscale input and to produce a 108-dimensional output.

A.3 Behavioral readout and feature-extraction details

Shared frozen-feature protocol. For each task, the trained neural-prediction model was placed in evaluation mode and all neural-prediction parameters were frozen. We generated synthetic train, validation, and test stimuli, extracted model features in batches, cached the resulting feature matrices on CPU, and trained only a task-specific linear probe. Within each run seed, synthetic train, validation, and test draws were matched across encoder architectures. Binary tasks used a one-logit linear probe trained with binary cross-entropy, whereas multiclass tasks used a softmax linear probe trained with cross-entropy. The mouse-specific neural readout heads were not used by task probes.

Task-specific feature convention. Static Orientation task used the final visual-encoder output. Each static grating image was passed directly through the model’s visual encoder, yielding a feature matrix $X \in \mathbb{R}^{N \times 108}$. The GRU was constructed when loading the checkpoint but was not used for Orientation feature extraction.

Dynamic Contrast and Motion RDK tasks used GRU features. Dynamic Contrast extracted the final GRU hidden state from a five-frame clip, giving a feature matrix $X \in \mathbb{R}^{N \times 512}$. Motion RDK first reshaped each 80-frame clip into 16 non-overlapping chunks of five frames, extracted the last GRU state for each chunk, and then used the final chunk state as the clip-level feature; this also yielded $X \in \mathbb{R}^{N \times 512}$. Static Orientation and Dynamic Contrast used raw features, whereas Motion

RDK applied feature standardization using training-set statistics. We standardized Motion RDK features because the recurrent clip-level features showed substantially larger across-clip variance, and unstandardized linear probes did not reliably converge.

Static Orientation task details. Orientation stimuli were full-field sinusoidal gratings rendered at 60×80 pixels. The task used 8 orientation classes spanning $[0^\circ, 180^\circ)$, with orientations sampled continuously within each bin. The probe was trained to predict the orientation class from the 108-dimensional visual-encoder output. Chance performance was therefore $1/8$.

Training, validation, and in-distribution test stimuli were sampled from the same nuisance distribution. Spatial frequency was sampled from $\{0.02, 0.06, 0.10, 0.14, 0.18\}$ cycles per pixel; contrast from $\{0.70, 0.85, 1.00\}$; additive noise standard deviation from $\{0.00, 0.04, 0.08\}$; Gaussian blur σ from $\{0.00, 0.30, 0.60\}$; and mean luminance from $\{0.48, 0.50, 0.52\}$. Phase was sampled uniformly from $[0, 2\pi)$. The compound out-of-distribution test split used shifted nuisance values: spatial frequency $\{0.04, 0.08, 0.12, 0.16, 0.20\}$ cycles per pixel, contrast $\{0.55, 0.75, 0.95\}$, noise standard deviation $\{0.06, 0.08, 0.10\}$, blur $\sigma \in \{0.45, 0.60, 0.80, 1.00\}$, and mean luminance $\{0.46, 0.50, 0.54\}$.

For each architecture and run seed, probes were trained across a sample-efficiency sweep with training-set sizes

$$N_{\text{train}} \in \{25, 100, 250, 500, 1000, 2000, 5000, 10000, 20000\}.$$

The full training pool contained 20,000 samples, with 2,000 validation samples, 10,000 IID test samples, and 10,000 OOD test samples. The primary scalar endpoint for cross-model analyses was accuracy at the largest training-set size, computed separately for ID and OOD test splits. Normalized area under the accuracy curve as a function of $\log_{10}(N_{\text{train}})$, along with chance-adjusted AUC values, was exported as a secondary sample-efficiency summary.

Dynamic Contrast task details. Inspired by Glickfeld et al. [2013], the training clips contained either a flashed Gabor target or a blank noisy background. Targets were flashed in a fixed visual-field patch within a $120^\circ \times 90^\circ$ visual field mapped to the model’s 60×80 input grid; training also included nuisance variation in background noise, carrier spatial frequency, and blur. Target contrasts for probe training were sampled from $\{0.05, 0.08, 0.12, 0.18, 0.27, 0.40, 0.60, 0.90, 1.0\}$. Evaluation used the contrast grid $\{0.00, 0.02, 0.04, 0.06, 0.08, 0.10, 0.13, 0.17, 0.21, 0.27, 0.34, 0.44, 0.55, 0.70, 0.90, 1.0\}$. Positive examples flashed the target on one of the last three frames of the five-frame clip. Feature standardization was disabled for this task. For each contrast c , balanced accuracy was computed as

$$\text{BA}(c) = \frac{1}{2} [\text{hit rate}(c) + \text{correct rejection rate}],$$

where the correct-rejection rate was estimated from blank trials. The primary summary was normalized area under the $\text{BA}(c)$ curve.

Motion RDK task details. Inspired by Stirman et al. [2016], the motion stimuli were 80-frame random-dot kinematogram clips with dot lifetime $\tau = 20$. The probe was trained on high-coherence conditions $\{0.95, 0.87, 0.79, 0.71, 0.63\}$ and evaluated on the coherence grid $\{0.00, 0.08, 0.16, 0.24, 0.32, 0.40, 0.48, 0.56, 0.64, 0.72, 0.80, 0.88, 0.95\}$. Feature standardization was enabled: the training-set feature mean and standard deviation were estimated once per architecture and run seed and then reused for validation and testing. The primary summary was normalized area under the accuracy-versus-coherence curve.

A.4 Emergent tuning and representation-geometry details

Feature space. Emergent tuning was measured at the final visual-encoder output of each trained model. For a static image $\mathbf{x} \in \mathbb{R}^{1 \times 60 \times 80}$, the frozen visual encoder produced a feature vector

$$\mathbf{z} = f_\theta(\mathbf{x}) \in \mathbb{R}^{108}.$$

Each dimension of this vector was treated as a latent feature unit. This final 108-dimensional visual-encoder output has no explicit spatial layout, so units were indexed only by feature dimension. Because these encoder dimensions are signed model features rather than nonnegative firing rates, all tuning summaries in this section (orientation selectivity, phase modulation, and contrast-response fits) use signed-feature variants of the corresponding metrics, as detailed below.

Stimuli. We probed each model with static full-field sinusoidal gratings rendered at the same spatial resolution as the neural-prediction movies, 60×80 pixels. We characterized latent-unit tuning using fixed grids of full-field sinusoidal gratings varying orientation, spatial phase, spatial frequency, and contrast, inspired by classical mouse V1 grating-tuning assays and recent CNN unit-tuning analyses [Ringach et al., 2016, Jang and Tong, 2024]. For pixel coordinates (x, y) , orientation θ , spatial frequency f in cycles per pixel, phase ϕ , contrast c , and mean luminance $\mu = 0.5$, the stimulus intensity was

$$I(x, y) = \mu + \frac{c}{2} \sin(2\pi f(x \cos \theta + y \sin \theta) + \phi),$$

clipped to the interval $[0, 1]$. The main orientation–phase–spatial-frequency grid used contrast $c = 1.0$, 16 orientations uniformly spaced over $[0^\circ, 180^\circ)$, 16 phases uniformly spaced over $[0, 2\pi)$, and 8 log-spaced spatial frequencies from 0.01 to 0.32 cycles per pixel. Contrast curves were measured on the grid

$$c \in \{0.00, 0.02, 0.04, 0.08, 0.16, 0.32, 0.64, 1.00\}.$$

Orientation, spatial-frequency, and phase curves. For each architecture and run seed, we first evaluated the visual encoder on the full orientation–phase–spatial-frequency grid. This produced a response tensor

$$R_{o,p,s,u},$$

where o indexes orientation, p indexes phase, s indexes spatial frequency, and u indexes the visual-encoder feature dimension. Orientation tuning curves were computed by averaging over phase and spatial frequency:

$$R_{u,o}^{\text{ori}} = \frac{1}{PS} \sum_{p=1}^P \sum_{s=1}^S R_{o,p,s,u}.$$

Orientation selectivity was computed after baseline subtraction. Specifically, we defined

$$r_{u,o} = R_{u,o}^{\text{ori}} - \min_{o'} R_{u,o'}^{\text{ori}},$$

and computed global orientation selectivity as

$$\text{gOSI}_u = \frac{|\sum_o r_{u,o} \exp(2i\theta_o)|}{\sum_o |r_{u,o}|}.$$

The corresponding vector-based preferred orientation was

$$\theta_u^* = \frac{1}{2} \arg \left(\sum_o r_{u,o} \exp(2i\theta_o) \right) \pmod{180^\circ}.$$

For the subsequent spatial-frequency and phase analyses, we used each unit’s preferred discrete orientation bin from the sampled grid. Spatial-frequency curves were computed at this preferred orientation by averaging over phase:

$$R_{u,s}^{\text{sf}} = \frac{1}{P} \sum_{p=1}^P R_{o_u^*,p,s,u}.$$

Spatial-frequency preference was summarized in both sampled-grid and fitted forms. The sampled-grid estimate was defined as the spatial frequency with maximal response on $R_{u,s}^{\text{sf}}$. In addition, we fit each unit’s spatial-frequency curve with a seven-parameter difference-of-Gaussians (DoG) function in log-spatial-frequency space. For $x = \log_2(f)$, where f is spatial frequency in cycles per pixel, the fitted curve was

$$\hat{R}_u(f) = R_0 + A_{\text{exc}} \exp \left[-\frac{1}{2} \left(\frac{x - \mu_{\text{exc}}}{\sigma_{\text{exc}}} \right)^2 \right] - A_{\text{inh}} \exp \left[-\frac{1}{2} \left(\frac{x - \mu_{\text{inh}}}{\sigma_{\text{inh}}} \right)^2 \right],$$

with nonnegative excitatory and inhibitory amplitudes. Fits were initialized from five starting points, and the solution with the largest R^2 on the sampled response curve was retained. The fitted preferred spatial frequency was defined as the maximum of the fitted DoG curve on a dense geometrically spaced grid spanning the sampled spatial-frequency range. A fit was considered usable when it

succeeded, produced finite fit values, and satisfied $R^2 \geq 0.10$. The primary preferred-SF metadata column used the fitted preferred spatial frequency; the sampled-grid and fit-only preferred SF values were also retained as separate metadata columns. The sampled-grid preferred-SF index was retained for operations requiring an index into the measured response tensor, including phase and contrast curve extraction.

Phase curves were then computed at each unit’s preferred discrete orientation and preferred discrete spatial frequency:

$$R_{u,p}^{\text{phase}} = R_{o_u^*, p, s_u^*, u}.$$

Phase modulation was summarized using the ratio of first-harmonic amplitude to the absolute DC component of the phase curve,

$$F1/F0_u = \frac{2|\widehat{R}_{u,1}|}{\max(|\widehat{R}_{u,0}|, \epsilon)},$$

where $\widehat{R}_{u,k}$ denotes the discrete Fourier coefficient of the phase curve and $\epsilon = 10^{-6}$ prevents division by zero. The preferred phase was defined as the phase angle of the first Fourier component.

Contrast-response curves. Contrast tuning was measured at each unit’s preferred orientation and preferred spatial frequency. To avoid redundant forward passes, units sharing the same preferred orientation–spatial-frequency pair were grouped together. For each unique pair, we rendered gratings across the contrast grid and all phase values, extracted responses from the final 108-dimensional visual-encoder output, and averaged over phase:

$$R_{u,c}^{\text{contrast}} = \frac{1}{P} \sum_{p=1}^P R_{c,p,u|o_u^*, s_u^*}.$$

Each contrast curve was fit with a signed Naka–Rushton function,

$$R(c) = R_0 + R_{\text{max}} \frac{c^n}{c^n + C_{50}^n},$$

where R_0 is the baseline response, R_{max} is the response gain, C_{50} is the semisaturation contrast, and n is the exponent. Consistent with the signed-feature convention noted above, the gain parameter R_{max} was allowed to be positive or negative. Fits were summarized by R_0 , R_{max} , C_{50} , n , and coefficient of determination R^2 .

Quality-control flags. Quality-control flags were used to identify units with measurable tuning for summary analyses. A unit was considered responsive if the maximum peak-to-peak response across its orientation, phase, spatial-frequency, and contrast curves exceeded 10^{-6} . Orientation QC required responsiveness, finite gOSI, and an orientation response range above 10^{-6} . Phase QC required responsiveness, finite F1/F0, and a phase response range above 10^{-6} . Spatial-frequency QC required responsiveness, a spatial-frequency response range above 10^{-6} , a finite preferred spatial frequency, and an acceptable DoG fit with finite fitted preferred SF and $R^2 \geq 0.10$. Contrast QC required responsiveness, a contrast response range above 10^{-6} , a finite Naka–Rushton fit, and fit quality $R^2 \geq 0.10$. These thresholds were used as loose inclusion criteria for descriptive summaries, not as claims that the corresponding features are biological neurons.

Saved tuning summaries. For each architecture and run seed, the emergent tuning pipeline saved a unit-level metadata table containing one row per visual encoder output feature dimension, including orientation preference and gOSI, phase F1/F0, sampled-grid and DoG-fitted spatial-frequency preference and bandwidth summaries, contrast-fit parameters, and QC flags. The full orientation, phase, spatial-frequency, and contrast response curves were also cached. Cross-model analyses used aggregate summaries derived from these unit-level metadata tables.

Representation eigenspectrum. For each trained model, representation geometry was summarized by fitting a power law to the eigenspectrum of hidden activity. This analysis used a fixed reference mouse session, 070921_J553RT, sampling 5,000 clips from the concatenated train and test segments. For each clip, we extracted the final GRU hidden state, standardized each feature dimension across clips, and applied PCA, retaining up to 256 components capped by feature dimensionality and sample

count minus one. The eigenspectrum exponent α was estimated by linear regression in log–log coordinates over the predefined rank window 20–200, with α defined as the negative slope of the fitted line. The same procedure was applied to the visual-encoder output for diagnostic purposes; only the final-GRU exponent was used as the representation-geometry column in the cross-model analyses.

A.5 Cross-model statistical analysis details

The cross-model analysis related neural-prediction performance, behavioral readout performance, emergent tuning, and representation geometry across the model zoo. Because the neural-prediction objective, recurrent architecture, and mouse-specific readout structure were held fixed while the visual encoder architecture varied, cross-architecture variation provided the substrate for asking how these axes covaried. These analyses were descriptive and associational rather than causal: they tested whether architectural differences that affected neural prediction aligned with task readout performance, tuning structure, or population geometry.

For each run seed s and architecture a , the scatter-analysis table combined four classes of quantities. First, neural-prediction performance was read from held-out mouse-response prediction summaries, including mean prediction correlation across the included mouse data. Second, behavioral readout metrics were read from task-specific summary files: Orientation accuracy at the largest training-set size, Dynamic Contrast balanced-accuracy AUC, and Motion RDK accuracy AUC. Third, emergent tuning summaries were computed from the visual-encoder tuning analysis, including summary orientation selectivity, phase modulation, and contrast semisaturation. Fourth, representation-geometry quantities, including the GRU eigenspectrum exponent, were merged for the same seed and architecture.

The final statistical table had one row per (s, a) pair before aggregation. Headline scatter plots used architecture-level means,

$$\bar{x}_a = \frac{1}{S} \sum_{s=1}^S x_{s,a},$$

with $S = 3$ run seeds. When shown, uncertainty bars reflected variability across run seeds. Pairwise scatter panels were generated for a predefined set of cross-axis relationships: neural prediction versus task performance; neural prediction versus emergent tuning; neural prediction versus representation geometry; representation geometry versus task performance; and emergent tuning versus task performance. Each panel reported a fitted linear trend and an associated correlation or regression statistic.

A.6 Computational resources

All models were implemented in PyTorch and run on single-GPU workstations using NVIDIA RTX 4090 GPUs with 24 GB memory and NVIDIA RTX 5060 Ti GPUs with 16 GB memory. Across architectures, the full evaluation pipeline for a single architecture took approximately 1–5 hours to run, including feature extraction, visual readout evaluation, latent-unit tuning analyses, population-geometry analyses, and summary-statistic generation.

B Model Neural Prediction and Task Performance

Table 2: Model Neural and Task Performance Metrics. Mean \pm cross-neuron SD for neural prediction and Mean \pm cross-seed SD for task performances.

Model	Neural Prediction	Orientation	Contrast	RDK
AlexNet	0.458 \pm 0.160	0.405 \pm 0.085	0.865 \pm 0.033	0.545 \pm 0.009
Xu et al. [2023]	0.527 \pm 0.154	0.776 \pm 0.022	0.908 \pm 0.020	0.557 \pm 0.003
EfficientNet	0.466 \pm 0.166	0.548 \pm 0.043	0.880 \pm 0.026	0.514 \pm 0.014
MobileNet	0.473 \pm 0.166	0.620 \pm 0.027	0.820 \pm 0.057	0.505 \pm 0.005
RegNet	0.461 \pm 0.158	0.601 \pm 0.049	0.785 \pm 0.083	0.506 \pm 0.005
ResNet	0.484 \pm 0.159	0.615 \pm 0.048	0.868 \pm 0.046	0.515 \pm 0.006
ShuffleNet	0.394 \pm 0.161	0.411 \pm 0.052	0.704 \pm 0.032	0.510 \pm 0.006
SqueezeNet	0.533 \pm 0.157	0.614 \pm 0.091	0.906 \pm 0.024	0.562 \pm 0.022